Hindawi
Advances in Civil Engineering
Volume 2019, Article ID 1542797, 14 pages
https://doi.org/10.1155/2019/1542797

Research Article

Numerical Simulation and Microscopic Stress Mechanism for the Microscopic Pore Deformation during Soil Compression

Gaoliang Tao, Wan Peng, Henglin Xiao, Xiaokang Wu, and Yin Chen

Hubei Provincial Ecological Road Engineering Technology Research Center, Hubei University of Technology, Wuhan 430068, China

Correspondence should be addressed to Henglin Xiao; xiao-henglin@163.com

Received 18 December 2018; Revised 14 January 2019; Accepted 23 January 2019; Published 3 March 2019

Academic Editor: Yinshan Tang

Pore structure is closely related with strength, constitutive relation, consolidation characteristics, and permeability properties of soil. Consequently, improving the understanding of the relationship between microscopic structure and macroscopic physical and mechanical properties has extremely important scientific significance. A large number of studies have shown that pores of soil have fractal features, and hence, the carpet model can be used to approximately simulate the fractal structure of clay. In the present study, ANSYS software was selected to establish a microscopic model of clay to study the distribution of microscopic stress and microscopic deformation characteristics of pores under different consolidation pressures. Besides, the variation law of microscopic pore size was quantitatively determined by using IPP (Image-Pro Plus) software. Combined with the fractal theory, the changes of microscopic pore of numerical simulation and that of physical experiment during compression of clay are studied. All the results indicated that the microscopic stress distribution of clay is not uniform on the compaction process. The larger the pore size is, the bigger the compression stress on both sides and the greater the bending deformation of upper part of the pore is, which leads to the deformation of larger pores which is bigger than that of smaller pores. Based on the results, issues about the microscopic mechanism of the difference in vertical and horizontal permeability under compression of clay, the relationship between the changes of pore shape and microscopic stress, the preliminary principle of "preferential crush of larger particles" for granular soil, skeleton stress across the region where stiffness is relative larger, and the self-protection of particles and pores are also discussed. The results of this study are of great importance in understanding of soil compression and related physical and mechanical properties from the microscopic view.

1. Introduction

Soil is made up of different particles formed by weathering of continuous and hard rock. Through different transport methods, those particles accumulate, among which massive pores exist. So, the structure of soil is complex and diverse. The microscopic structure of soil has direct influence on the strength, consolidation characteristics, and permeability properties, which are of great significance to the study of microscopic structure of soil. Gylland et al. [1] studied the effect of microstructural changes of clay on shear strength. Zhang et al. [2] applied a digital imaging method to investigate the evolution of microscopic pore of soft clay in the process of consolidation, and it was found that the consolidation process has an effect of adjusting on the gradation of microscopic pores. Zhang et al. [3] measured the pore water pressure of sandy soil and silty clay in laboratory during freeze-thaw cycles to study the influence on physical and mechanical properties of soils. Tan et al. [4] proposed a permeability model for porous media by considering the stress sensitivity. Liu et al. [5] established a model on the relationship between relative equivalent permeability and fractal dimension of a fractured rock mass under the triaxial stresses and fluid-rock reactions, and it was determined that the relative equivalent permeability changes with the variations in fractal dimension. Lei et al. [6] conducted laboratory tests to study the effect of pressure condition on stress dependency of relative permeability curves and derived a corresponding fractal model for the stress-dependent relative permeability to interpret the experimental results.

Terzighi [7] proposed the concept of microscopic structure of clay soil in 1925. With the development of science and technology, the means of observation for microscopic structure are more abundant and reliable. A large number of studies have been carried out on the microscopic structure of soil. Wu [8] quantitatively determined the distribution of clay particles by computer image processing. By using light microscopy, Cox and Budhu [9] investigated a practical approach to quantify grain shape and identify the key shape parameters that can distinguish grains. Tarantino and De Col [10] described pore-size distributions of compacted samples through MIP (mercury intrusion porosimetry) tests. Arnepalli et al. [11] determined specific surface area of fine-grained soils through the MIP test and attempted to develop relationships between the basic properties of fine-grained soils and specific surface area. Oualmakran et al. [12] measured pore-size distributions at different states of soil by using the MIP test and investigated the effects of compaction water content, drying techniques adopted prior to performing porosimetry, and saturation and loading on the evolution of the microscopic structure of a silty soil. Gao et al. [13] compared effects of different sampling methods (compaction-reconstitution) on hydromechanical behaviour of unsaturated soils by using the MIP test. Romero and Simms [14] attempted to describe the difference of hydromechanical behavioural features observed at a macroscopic scale by the MIP test and the environmental scanning electron microscopy (ESEM), respectively. By using MIP and SEM, Hattab et al. [15] described a microscopic structural evolution of a deep-water marine sediment with various stress paths. Zhang and Kong [16] analyzed the pore characteristics of offshore clay using the SEM method, MIP, and nitrogen adsorption method. Khalid et al. [17] investigated the effect of low cement content on the microstructure of soft clay by performing SEM and MIP tests. Stingaciu et al. [18] determined pore-size distributions and hydraulic properties of natural porous media by NMR relaxometry. Tomioka et al. [19] observed bentonite particles of compacted samples before and after water saturation by a newly developed X-ray microscopic CT having a high spatial resolution. Nie et al. [20] determined the microscopic structure to analyze the collapsibility of coarse-grained soil and explored the mechanism of collapsibility generation by carrying out SEM on coarse-grained soil in the Gobi region. Wang et al. [21] performed the tensile tests and SEM test to analyze changes of the loess microstructure in the tensile test. Matthew et al. [22] approximately simulated the behaviour of natural sand in undrained loading with calibration of virtual particles by using the discrete element method (DEM). Zhao et al. [23] simulated the true triaxial shear of granular soils by using the DEM and studied effects of the model on the macro- and micromechanical behaviours. Sufian et al. [24] characterized pore space properties from discrete element simulations of monodisperse particle assemblies in two-way cyclic shearing to study the deformation response of sheared granular assemblies. Farroukh et al. [25] performed some physical tests and microstructure observation (SEM and X-ray diffraction analyses) on clayey soils with Tunisian phosphogypsum to investigate soil responses in the presence of phosphogypsum at various proportions. Zainuddin et al. [26] studied the geotechnical properties of the marine clay by conducting mechanical tests and microstructural analysis tests (SEM and X-ray diffraction). Li et al. [27] interpreted the microstructural evolution of loess soils due to loading and wetting by using a MATLAB program to process the micrographs. However, above physical experiments can only analyze the overall change trend of soil pore but cannot track the variation law of a single pore accurately, and the microscopic mechanical mechanism of a single pore cannot be revealed yet.

A few physical experiments have been shown that the compaction process of clay soil mainly induced the compression deformation of large pores, which is called "preferential compression of large pore." Cuisinier and Laloui [28] found that suction increase produced a strong decrease in the large pores by using suction-controlled oedometer and MIP tests. Zhou and Mu [29] carried out strength tests on soft soil in the Pearl River Delta and studied the microscopic structure of pores on fracture surface by using SEM. The results showed that the large pores changed first and its volume decreased greatly under the action of external force in the soft soil. Zhang and Wang [30] quantitatively studied the pore-size distribution characteristics of soft soil in Huangshi area before and after creep by using SEM. It was found that the deformation of large pores was greater than that of small pores in the compression process. Tao et al. [31] studied the pore-size distribution of clay soil before and after compression deformation by using MIP, SEM, and nuclear magnetic resonance technique, respectively. It was found that, with the increase of dry density (i.e., the increase of the compaction degree), the compression deformation first caused the compression of the large pores and the total volume of the small pores corresponding to the unit particle mass was almost unchanged. Tan et al. [32] studied the pore-size distribution characteristics of Hunan red clay with different dry densities by using MIP. It was found that the pores with larger size have large change under compaction. As a result, under the action of external force, the variation law of internal pores of soil follows the principle of "preferential compression of large pore." This phenomenon might be of universal significance. However, more development should be promoted to investigate the internal mechanism of this phenomenon. Tao et al. [31] assumed that the structure of large pores was less stable than that of small pores, so large pores were compressed first. Qian et al. [33] considered that the mechanical structure of small pores was more stable because of the cementation state of inlaid pores and the electrical attraction between clay particles, which may be one of the reasons that leads to the first compression of large pores and the difficulty of compression of small pores. The explanation of these mechanisms is still in preliminary and requires more studies for this to be better understood and confirmed.

In this paper, the method of numerical simulation was used to study the variation laws of microscopic pores of clay, accurately trace the changes of shape and size of a single pore during compression, and reveal their microscopic stress

mechanism. The carpet model was used to approximately simulate the fractal structure of clay, and ANSYS software was selected to establish a microscopic model for the study of microscopic stress distribution and microscopic deformation characteristics of pores under different consolidation pressures. Besides, the variation law of microscopic pore size was quantitatively analyzed by using IPP software. In addition, the phenomenon of "preferential compression of large pores" was verified, and its internal mechanism was explained by theoretical analysis combined with the results of numerical simulation on distribution of microscopic stress. Based on the result, issues about the microscopic mechanism of the difference in vertical and horizontal permeability under compression, the relationship between the change of pore shape and microscopic stress, the preliminary principle of "preferential crush of larger particles" for granular soil, skeleton stress across the region where stiffness is relative larger, and the self-protection of particles and pores are also discussed.

2. Numerical Simulation

By the method of numerical simulation, the variation of distribution characteristics of pore during soil compaction is easy to be simulated and the microscopic mechanism can be revealed. However, due to the complexity of soil, the real pore structure is difficult to be exhibited in numerical simulation. Studies have shown that the pore-size distributions in soil have strong fractal features, so they can be approximately simulated by the carpet model [34–37]. In this paper, based on the carpet model, the microscopic model of clay was established by ANSYS software, and the distribution law of microscopic stress on compaction process was simulated. Combined with IPP technology, the variation law of pore distribution was analyzed. In addition to the emphasis on verifying the principle of "preferential compression of large pores," the internal mechanism of compression deformation of pores was revealed.

2.1. ANSYS Software and Model. ANSYS software is a large-scale and universal finite element analysis (FEA) software developed by ANSYS Company of USA. It is one of the fastest growing software of computer-aided engineering (CAE) in the world. In this paper, the pore-size distribution in clay was simulated by the carpet model. The diagram of the carpet model is shown in Figure 1. White parts represent the visible pores, while black parts represent the coexistence of invisible pores and clay grains. With the orders increasing (i.e., the observation scales decreasing), the pores of the black part gradually unfold from large to small. The model is easy to be established and relatively close to the pore structure. That is, the stress of large and small pores in soil can be approximately simulated.

It is a great advantage that most of the CAD files can be directly imported into ANSYS. Hence, in this paper, the carpet model is drawn by using CAD software firstly, and then the CAD file is imported into ANSYS. Taking the total side length of the unit as 1 mm, the above four order models

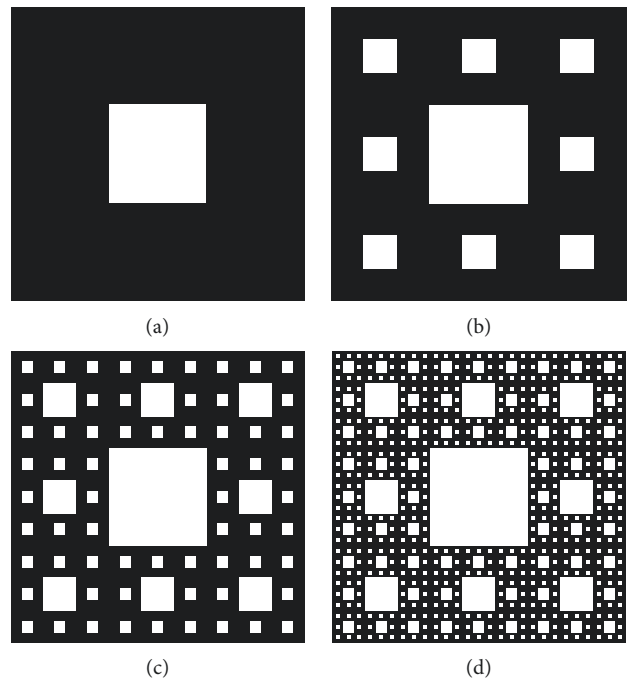

Figure 1: Carpet fractal models. (a) First-order model. (b) Second-order model. (c) Third-order model. (d) Fourth-order model.

are established, as shown in Figure 1. Then, the side lengths of pores with different sizes (from large to small) are 1/3 mm, 1/9 mm, 1/27 mm, and 1/81 mm, respectively.

2.2. Parameters and Loading of Model. The compression tests on clay were simulated by using ANSYS, and the property index of clay is shown in Table 1. A lateral constraint was applied on the left and right sides of the model, which only caused the deformation in the vertical direction. Meanwhile, the constraint was applied on the bottom of the model, which made the bottom fixed. It should be noted that two models were proposed here: one was the original carpet model, namely, large pore model. The other was the modified carpet model, namely, small pore model. In which, the small pore model was in the form of nine grooves; that is, the big pore in the center of the carpet model was replaced by the structures similar to surrounding. Above the large pore models, the applied consolidation loads were from 0 to 200 kPa (0, 50 kPa, 100 kPa, and 200 kPa). However, above the small pore models, the applied consolidation loads were from 0 to 400 kPa (0, 50 kPa, 100 kPa, 200 kPa, 400 kPa).

2.3. Analysis of Simulation Results. The CAD file was imported into ANSYS, parameters and constraints were set, and a uniform load was applied. By calculation and analysis, the deformation diagram, displacement nephogram, and stress distribution diagram under different load conditions were obtained, respectively. For the sake of simplicity, Figure 2 gives only the comparison between the deformation diagram of large and small pore models under 100 kPa pressure. The diagrams of the white background are the

Table 1: Property index of clay.

Cohesion force (kPa)	Internal friction angle (°)	Elastic modulus (MPa)	Unit weight (kN/m^3)	Poisson's ratio
38	18	7.4	20.2	0.2

original model of zero load, and those of black background are the deformation diagrams under 100 kPa pressure. As shown in Figure 2(b), the deformation of the small pore model is more uniform than that of the large pore model. As shown in Figure 2(a), the deformation of pores in the middle location is larger than that in the edge location. The displacement nephogram of large and small pore models under 100 kPa pressure is shown in Figure 3. The displacement of clay at different locations is represented by different colors. It is interesting to note that, at the same height, the displacement of the small pore model is approximately equal. Meanwhile, the displacement of the large pore model is larger than that of the small pore model at the same height. Furthermore, the displacement of bottom is much larger than that of above for two pore models.

2.4. IPP Software. The size, area, and area summation of pores in different levels in the picture can be measured by using IPP software. Due to the excessive levels and quantities of pores, it was not convenient to list them one by one. Therefore, some of the representative pores were selected and numbered, as shown in Figure 4. The specific steps for measuring the size and area of pores by IPP software are now elaborated as follows:

(1) For entering the interface to set the graphic scale, a new space calibration was created from the measurement menu. Then, millimeter was chosen as unit, and a length size of one millimeter was drawn on the diagram, which was consistent with the unit of model.

(2) There were two methods to outline the contour line of pores. One drew the line manually with mouse by the tester. The other drew the line by software. The contour line of this graph was very distinct, so it was automatically identified and completed by using a computer.

(3) The drawn contour line (i.e., AOI) was converted into the object by using the automatic measuring tool, and then the area was measured.

(4) The diameter and area of all the pores were measured, respectively, by using the automatic measurement method, and then a table was generated.

2.5. Measurement Results and Analysis of IPP. The microscopic deformation diagrams under different consolidation pressures calculated by using ANSYS software were extracted. Following the procedure presented previously, the changes of pore size and pore areas in the large pore model and small pore model under different pressures were measured by using IPP software. The compression law of pores was explained with the measurement results as shown in Tables 2 and 3, respectively.

Regardless of the large pore model or the small pore model, for a single specific pore, its size and area decreases with the increase in pressure as shown in Tables 2 and 3. However, the compression of large and small pores was significantly different, and the compression deformation of the large pores was much higher than that of small pores. In addition, the smaller the pore size was, the smaller the compression deformation was.

Pores with the same size in different positions had different compression. The deformation of small pores with the same size around large pores had great difference. Furthermore, the deformation of pores located on the oblique upper corner and two-side edges of the large pores were larger than that of pores located on the upper or lower. As for the minimum pores with the same initial pore size in Figure 4(a), the deformations of pores on the side (i.e., 4d) and oblique upper corner (i.e., 4c) around the large pores are much larger than that of pores on the upper corner (i.e., 4b). As for Figure 4(b), the deformation of pores on the side (i.e., 3d) and the oblique upper corner (i.e., 3c) around the large pores are larger than that of pores on the upper corner (i.e., 3b). The deformations of pores with the same pore size at different heights are different after compression. As shown in Figure 4(a), the deformation of pores 2b is slightly larger than that of pore 2c although they have the same pore size. As it can be seen from Figure 4(b), the deformations of pores having same pore size (i.e., 1a and 1c) are different. Besides, the diameter of the bottom pores (i.e., 3e and 3f) is almost unchangeable under small pressure, which indicates that the deformation of above pores is slightly larger than that of inferior pores in the model.

Based on all the distribution data of pores, the cumulative pore-size distributions of the large pore model and small pore model under different pressures are shown in Figures 5 and 6, respectively. As a conclusion, it could be stated that the cumulative pore area decreases with the increase of pressure for the large and small pore models. However, the smaller the pore size is, the smaller the change of the corresponding cumulative pore area is, and the data points of accumulative area of minimum pore size under different pressure conditions almost overlap. Meanwhile, the larger the pore size is, the larger the total reduction of pore area is, and the difference of cumulative total area corresponding to the maximum pore size under different pressure conditions is most obvious. The variation law of different pore size is consistent with that of described previously, which proves the phenomenon of "preferential compression of large pores" and illustrates that the macroscopic compression deformation of clay is mainly occurred due to the compression of large pores.

It is interesting to note that, under the same pressure, the deformation of the small pore model was smaller than that of the large pore model, which indicated that the macroscopic deformation of soil is affected by the pore

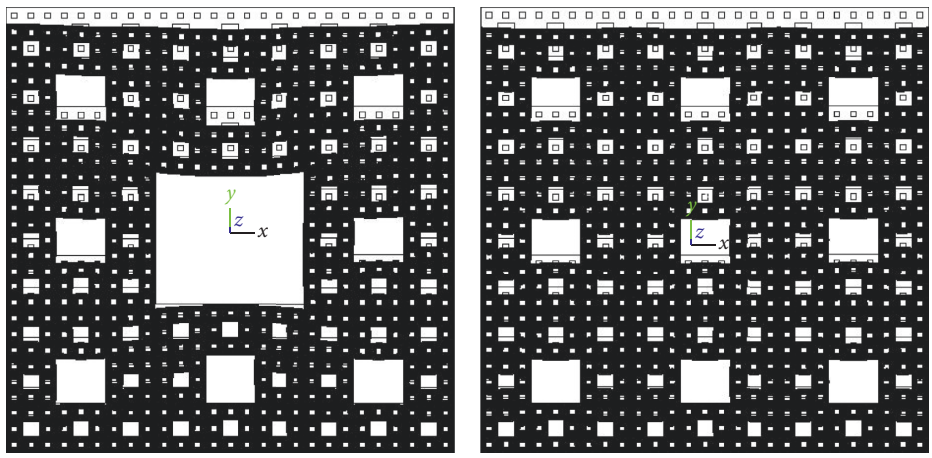

(a) (b)

Figure 2: Deformation diagram. (a) Large pore model. (b) Small pore model.

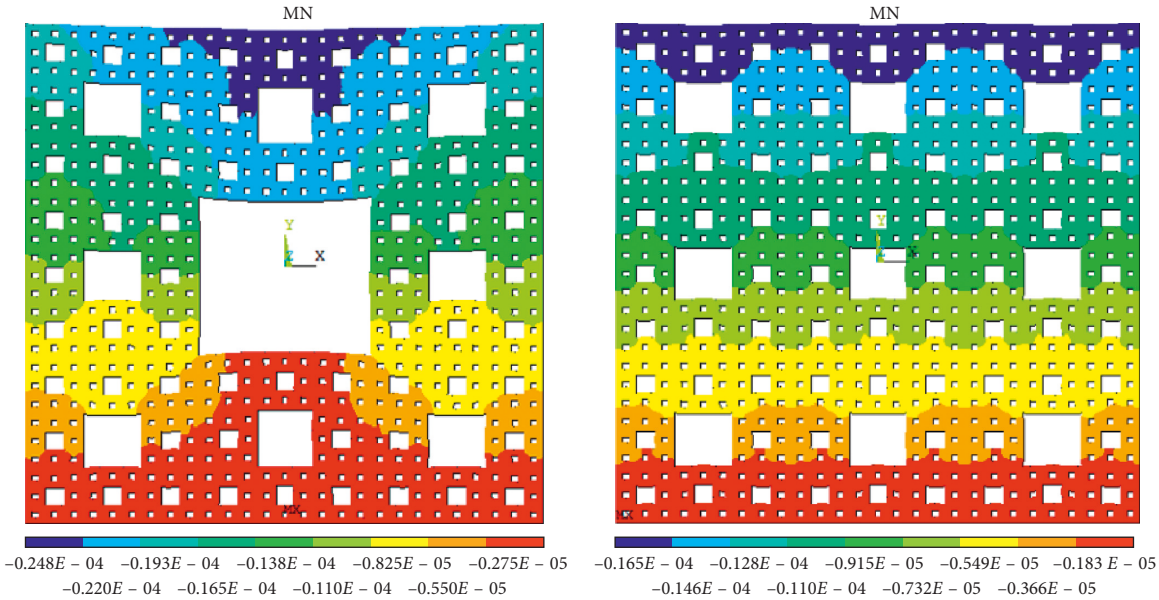

(a) (b)

Figure 3: Displacement nephogram. (a) Large pore model. (b) Small pore model.

structure. Specifically, the larger the dense of soil is, the smaller the compression is.

2.6. Comparison of Numerical Simulations and Experimental Results. Tao et al. [31] performed a series of consolidation experiments on undisturbed soft clay of Hanyi railway, and the specimens were taken under different consolidation pressures of $P = 0$, 50, 100, 200, 400, 800 kPa, respectively. Then, the experimental data were recorded. The specimens under different consolidation pressures were chosen to conduct the SEM tests. The SEM images of the soft clay specimens under different consolidation pressures were chosen as the research objects with a resolving power of 0.095 μm pixel^{-1}, and the research area was fixed at 127.8 μm × 95.8 μm. The SEM image segmentation into binary image of soft clay under different consolidation pressures was obtained as shown in Figure 7. The IPP image technique was used to perform the image processing and measure the size, area, and number of pores. The variation law of microscopic pore area of specimens under different consolidation pressures was obtained as shown in Figure 8.

It is shown in Figure 8 that corresponding to a certain particle area, the area of large pore changes greatly, with the increase of consolidation stress, while the accumulative area of the small pore is almost unchanged, and the accumulative pore area also presents a "broom-shaped" distribution as a whole.

As shown in Figures 5 and 6, respectively, under different pressures, the cumulative pore-size distributions of the large pore model and small pore model also present the "broom-shaped" distribution, and it is demonstrated that the

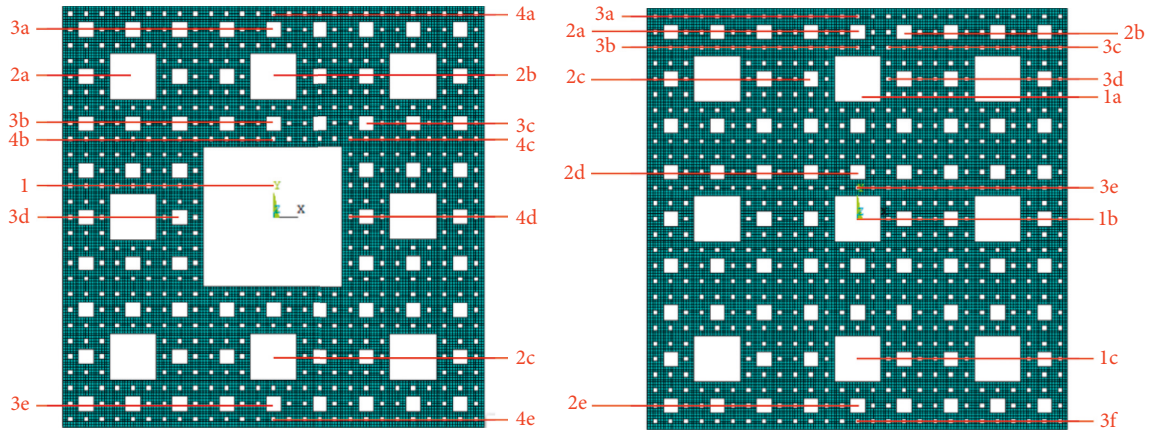

Figure 4: The number of pores in the model. (a) Large pore model. (b) Small pore model.

Table 2: The pore size and pore area of the large pore model under different pressures.

Number	0 kPa		50 kPa		100 kPa		200 kPa	
	Pore size	Pore area	Pore size	Pore area	Pore size	Pore area	Pore size	Pore area
1	0.333329	0.111108	0.322191	0.103807	0.313202	0.098095	0.291278	0.084843
2a	0.111108	0.012345	0.108267	0.011722	0.10551	0.011132	0.100657	0.010132
2b	0.111108	0.012345	0.110111	0.012124	0.106998	0.011449	0.104533	0.010927
2c	0.111108	0.012345	0.109547	0.012001	0.107057	0.011461	0.107253	0.011503
3a	0.036986	0.001368	0.035631	0.00127	0.036986	0.001368	0.034185	0.001169
3b	0.036986	0.001368	0.036641	0.001343	0.035413	0.001254	0.035008	0.001226
3c	0.036986	0.001368	0.034853	0.001215	0.035413	0.001254	0.03262	0.001064
3d	0.036986	0.001368	0.034723	0.001206	0.034735	0.001206	0.031734	0.001007
3e	0.036986	0.001368	0.036267	0.001315	0.036986	0.001368	0.035813	0.001283
4a	0.012288	0.000151	0.012046	0.000145	0.011617	0.000135	0.010650	0.000113
4b	0.012288	0.000151	0.012046	0.000145	0.011895	0.000141	0.011489	0.000132
4c	0.012288	0.000151	0.011662	0.000136	0.00922	0.000085	0.008062	0.000065
4d	0.012288	0.000151	0.011659	0.000136	0.011846	0.00014	0.009747	0.000095
4e	0.012288	0.000151	0.012046	0.000145	0.01149	0.000132	0.011075	0.000123

Table 3: The pore size and pore area of the small pore model under different pressures.

Number	0 kPa		50 kPa		100 kPa		200 kPa		400 kPa	
	Pore size	Pore area	Pore size	Pore area	Pore size	Pore area	Pore size	Pore area	Pore size	Pore area
1a	0.111108	0.012345	0.110172	0.012138	0.107032	0.011456	0.107032	0.011456	0.091018	0.008284
1b	0.111108	0.012345	0.110142	0.012131	0.108224	0.011712	0.108224	0.011712	0.092247	0.008510
1c	0.111108	0.012345	0.108382	0.011747	0.107231	0.011499	0.107231	0.011499	0.093028	0.008654
2a	0.036986	0.001368	0.036986	0.001368	0.036760	0.001351	0.036760	0.001351	0.036145	0.001306
2b	0.036986	0.001368	0.038631	0.001492	0.037404	0.001399	0.037404	0.001399	0.032148	0.001034
2c	0.036986	0.001368	0.035412	0.001254	0.035412	0.001254	0.035412	0.001254	0.030923	0.000956
2d	0.036986	0.001368	0.036857	0.001358	0.038373	0.001473	0.038373	0.001473	0.035750	0.001278
2e	0.036986	0.001368	0.036986	0.001368	0.036986	0.001368	0.036986	0.001368	0.034346	0.001180
3a	0.012288	0.000151	0.012288	0.000151	0.012288	0.000151	0.012288	0.000151	0.011236	0.000126
3b	0.012288	0.000151	0.012288	0.000151	0.012288	0.000151	0.012288	0.000151	0.011489	0.000132
3c	0.012288	0.000151	0.011761	0.000138	0.012288	0.000151	0.012288	0.000151	0.011411	0.000130
3d	0.012288	0.000151	0.012288	0.000151	0.012288	0.000151	0.012288	0.000151	0.011411	0.000130
3e	0.012288	0.000151	0.012288	0.000151	0.012288	0.000151	0.012288	0.000151	0.011912	0.000142
3f	0.012288	0.000151	0.012288	0.000151	0.012288	0.000151	0.012288	0.000151	0.011912	0.000142

predictions of the model exhibit similar variation trends as the experimental data, which verified that the Sierpiński carpet model can approximately simulate the pore distribution of natural clay.

2.7. Fractal Property of the Model. Yu and Li [35] deduced a unified fractal model based on the basic fractal theory. In their study, the relation between the fractal dimension D_f and porosity ϕ was obtained by

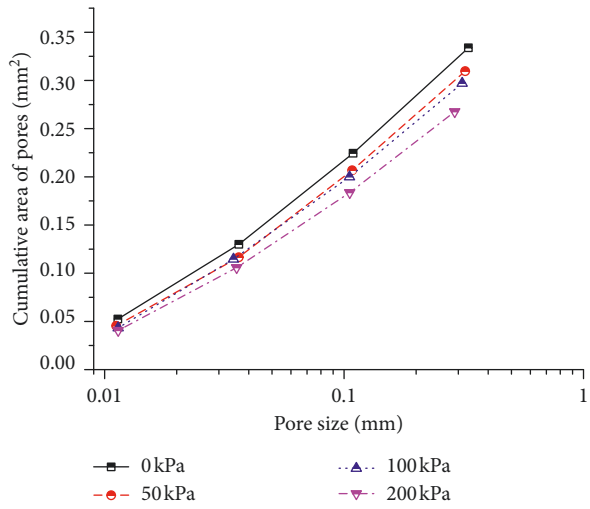

Figure 5: Cumulative pore-size distribution of the large pore model under different pressures.

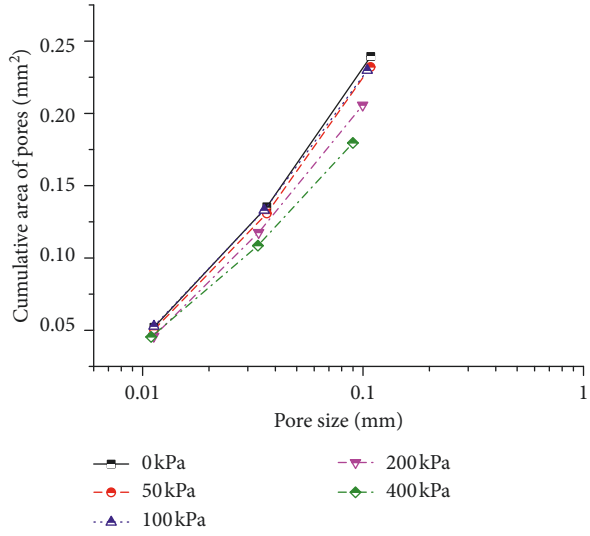

Figure 6: Cumulative pore-size distribution of the small pore model under different pressures.

$$D_f = 2 - \frac{\ln \phi}{\ln(\lambda_{min}/\lambda_{max})}, \quad (1)$$

where λ_{min} and λ_{max} are the lower and upper limits of self-similar regions, respectively. It should be highlighted that the particles were used as the research subject in the fractal model. However in this paper, the pores were used as the research subject, resulting that when the fractal dimension D_f is calculate, the porosity ϕ should be replaced by $1 - \phi$.

Variations of strain with stress, variations of fractal dimension with stress, and relationships between strain and fractal dimension were obtained as shown in Figures 9–11, respectively.

As can be seen in Figures 9–11, the strain and fractal dimension increased with the increase of stress. More precisely, the larger the stress was, the larger the compression was, and the pore area would be decreased, resulting in the proportion of particles increasing. Therefore, the fractal dimension would increase with the increase of stress. Furthermore, the fractal dimension has an approximately linear relationship with the strain, which shows that the fractal dimension can be the deformation parameter of soil during compression. Figures 9–11 also illustrate that the results of numerical simulation exhibit similar variation trends as the experimental data, which verified that the Sierpiński carpet model can approximately simulate the pore distribution of natural clay.

3. Mechanism of Microscopic Stress

To briefly analyze the microscopic mechanism of the phenomenon of "preferential compression of large pores," the further interpretations were carried out on the basis of the stress diagram obtained from the ANSYS numerical simulation. For the sake of simplicity, only the distribution diagrams of microscopic stress of the large pore model and small pore model under the pressure of 100 kPa are shown in Figures 12 and 13, respectively.

As shown in Figures 12 and 13, the microscopic stress of the two models was not uniform and the stress distribution around the pores with different sizes was quite different from the color distribution. In general, the compression stresses on both sides of large pores were larger than those of small pores in part ①, which was the one of internal reasons that the large pores is compressed preferentially.

Meanwhile, after large pores producing larger deformation, the "distribution of arch stress" occurred in the upper part of the large pore, as shown in the part ② of Figures 12 and 13. Owing to the stress distribution, the larger deformation of clay occurring at the collapsed large pores was also avoided. It can be seen that the parts of soil grains at the sides of large pores undertook most stress than those on the upper and lower parts of large pores. These stress distribution laws also resulted in that the deformation of the small pores on the side of the large pores was higher than that of pores on the upper part.

On the contrary, because the large pores have larger horizontal spans, the overall vertical displacement on the upper part of the pore was much larger than that on the both sides of pores under the same load conditions. For example, as shown in Figure 3(a), the differential displacement between the upper part and the two sides of the largest pore was very obvious, which resulted in a further reduction of the area of large pores.

The principle of compression of large pores was similar to the opinion that a large pore can be regarded as a "building," and then the adjacent soil on both sides could be seen as a "vertical member," while the upper soil could be taken as a "horizontal member," and the space size of soil was affected by the compression of "horizontal member" and the bending of "vertical member."

In addition, the main transmittal way of microscopic stress is shown in part ③ of Figure 13, where the effect of "skeleton stress" was obvious. More precisely, the stiffness of soil in the area of large pores was smaller than that of small

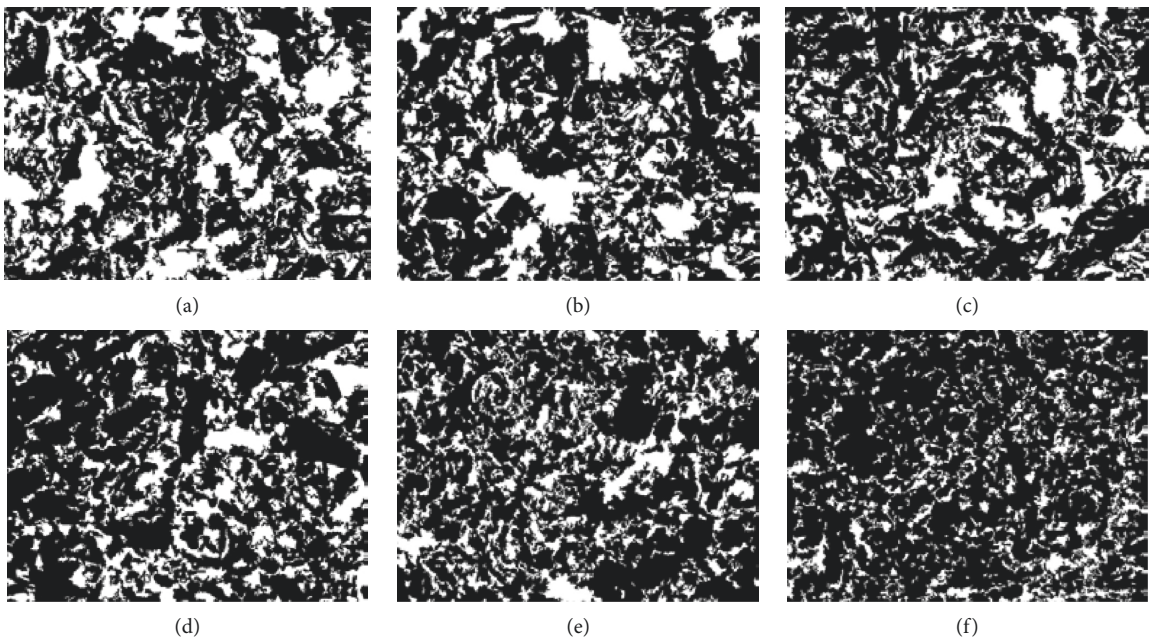

Figure 7: The SEM image segmentation into binary image of soft clay under different consolidation pressures: (a) 0 kPa; (b) 50 kPa; (c) 100 kPa; (d) 200 kPa; (e) 400 kPa; (f) 800 kPa (data after Tao et al. [31]).

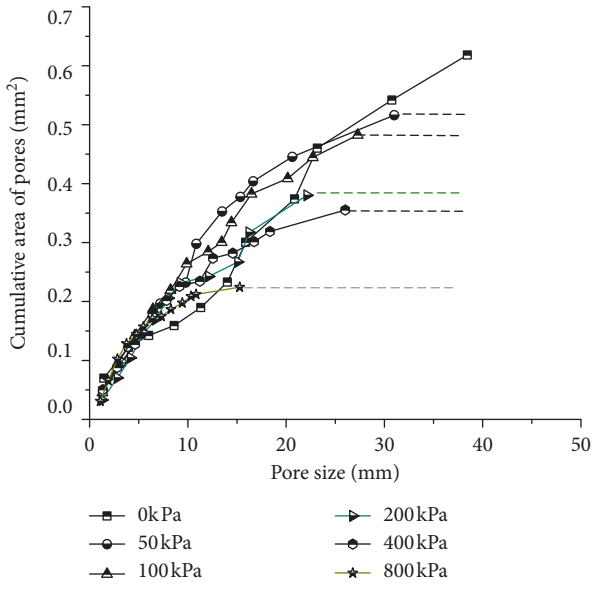

Figure 8: The variation law of microscopic pore area of specimens under different consolidation pressures (data after Tao et al. [31]).

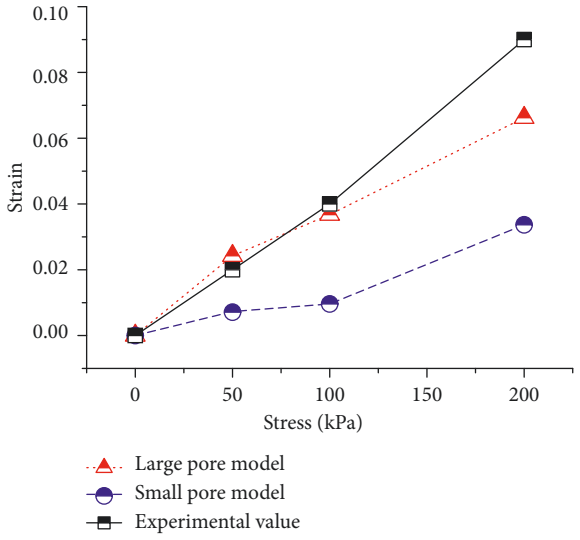

Figure 9: Comparison between the experimental and predicted strain under different pressures.

pores, which resulted in the selection of part ③ to bear the "skeleton stress." This kind of stress transfer path was a natural choice.

In order to further analyze the intrinsic mechanism of the microscopic stress distribution, it was assumed that there exists a maximum pore in the soil (such as the white area in Figure 14(a)), and the large pore size is taken as the observation scale, while the internal pores in the other regions cannot be identified. It is the coexisting part of soil grains and pores (such as the dark gray area in Figure 14(a)), and the whole analytical unit is called the "large pore unit." It was also assumed that the elastic modulus of the white pore is E_1 (assuming the pore filled with water and its elastic modulus is very small, which approximately approaches zero) and that of the dark gray part is E_2 ($E_2 \gg E_1$). The element is divided into three columns; as shown in Figure 14(b), the dark gray parts on the sides of the unit are merged (i.e., part A) and defined as the relative rigid region. The middle column (i.e., part B: including maximum pore in the middle and the dark gray part of the middle column) is defined as the relative flexible region and is represented by the light gray area in Figure 14(b).

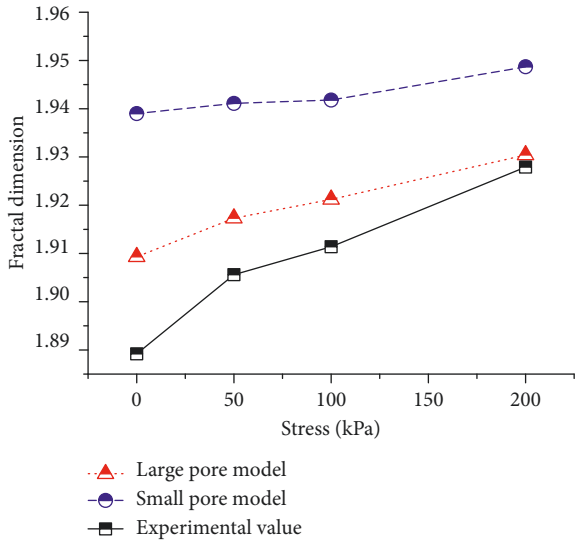

Figure 10: Comparison between the experimental and predicted fractal dimensions under different pressures.

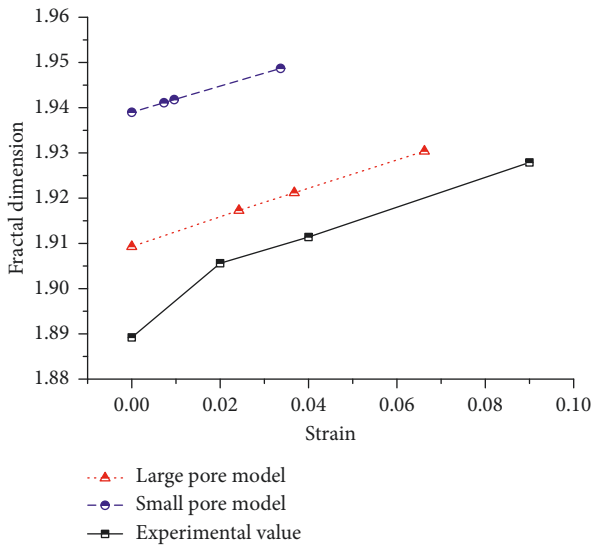

Figure 11: Relationships between strain and fractal dimensions.

It is assumed that, under external load, the compression deformation of the relative rigid region is equal to that of the relative flexible region, and the shear stress between them is ignored. If the unit uniform stress is applied to the upper part of the whole element, the stress of the relative rigid zone σ_r can be expressed as

$$\sigma_r = \frac{(A_r + A_f)\cdot 1}{E_r A_r + E_f A_f} E_r = \frac{1 + (A_f/A_r)}{1 + ((E_f A_f)/(E_r A_r))}, \quad (2)$$

where A_r is the cross-sectional area of the relatively rigid region, A_f is the cross-sectional area of the relatively flexible region, and E_r is the elastic modulus of the relatively rigid region, and E_f is the elastic modulus of the relatively flexible region. Likewise, the stress of the relative flexible zone σ_f is written as

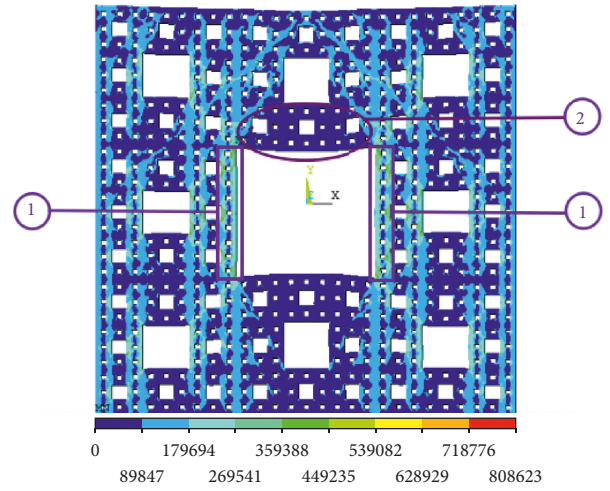

Figure 12: Stress distribution diagram of the large pore model.

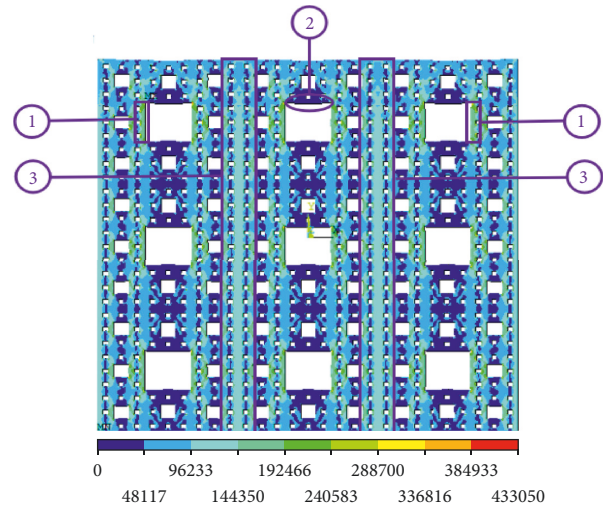

Figure 13: Stress distribution diagram of the small pore model.

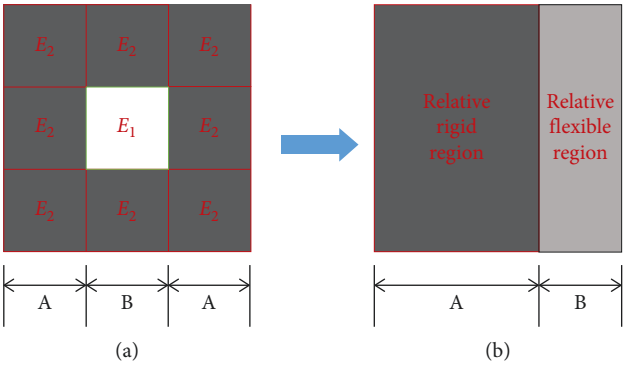

Figure 14: Large pore elements.

$$\sigma_f = \frac{1 + (A_r/A_f)}{1 + (E_r/E_f)\cdot(A_r/A_f)}. \quad (3)$$

The elastic modulus of E_r and E_f can be described as

$$E_r = E_2, \tag{4}$$

$$E_f = \frac{1}{\left((2/E_2)\Delta l + (1/E_1)\cdot\Delta l\right)/(3\cdot\Delta l)} = \frac{1}{(2/3E_2) + (1/3E_1)} = \frac{3E_1E_2}{2E_1 + E_2} = \frac{3E_1}{2(E_1/E_2) + 1}, \tag{5}$$

where Δl is the length of each small unit, as shown in Figure 14. Since $E_1 \ll E_2$, equation (5) can be approximately written as

$$E_f \approx 3E_1. \tag{6}$$

It is interesting to note that the ratio of E_f to E_r is very small and negligible. Therefore, equation (2) can be then simplified to

$$\sigma_r \approx 1 + \frac{A_f}{A_r}. \tag{7}$$

As can be seen in Figure 9, the larger the area of white pores is (i.e., the larger the pore size is), the larger the cross-sectional area of the relative flexible region A_f is (i.e., the larger the ratio of A_f to A_r is). By the inspection of equation (7), the stress of the relative rigid region σ_r is larger. In other words, the larger the pore size was, the greater the stress on both sides of the pore was, the greater the compression deformation was, and the greater the "bending" of the upper part of the pore was. Consequently, large pores compressed prior to small pores.

4. Discussion

4.1. Microscopic Interpretation of Differences in Permeability between Vertical and Horizontal under Compression Deformation. Wang et al. [38] carried out permeability tests on undisturbed loess by using triaxial permeability apparatus GDS, which measured the horizontal and vertical permeability coefficients under different dry densities. It was found that the permeability coefficient of horizontal was greater than that of vertical, and the permeability coefficient in both directions decreased with the increase of dry density. These laws can be preliminarily explained by the variation law of pore after compression deformation presented previously.

Firstly, combined with the basic theory of fluid mechanics, all the pores tended to decrease with the increase of pressure and the permeability coefficient of horizontal and vertical decreased accordingly. As was mentioned above, it was found that the compression of pores in the upper part of the model was slightly larger than that of pores in the lower part, which resulted in the more obvious effect of the upper pore on the permeability coefficient. Meanwhile, all the vertical pore channels and the upper horizontal pore channels were strongly affected by the upper pores, and the lower horizontal pore channels were less effected. Therefore, the permeability coefficient of the vertical part decreased more severely under the same compaction degree.

4.2. Variation of Pore Shape. Based on the numerical simulation and its results, it was found that the variation of pore shape was different in different positions under pressure. As shown in Figure 15, the shape of the pores in the upper part of the large pore (i.e., part a) remained basically unchanged because the corresponding stress was small. However, the shape of pores in the oblique upper corner of the large pore (i.e., parts b and c) changed from the initial square to parallelogram because the corresponding shear stress was large (noted that the subsidence displacement of the element above the large pore was larger than that of the element on both sides, as shown in Figure 3). In addition, the pores near the two sides of the large pore (i.e., parts d and e) changed from the original square to approximately rectangular; owing to the larger pressure, the deformation of the pore was mainly controlled by the compression of the soil on both sides of the pore.

4.3. Stress Mechanical Discussion of "Preferential Crush of Large Particles". Under the action of the external load, clay soils followed the principle of "preferential compression of large pores" and the granular geotechnical material followed the similar principle of "preferential crush of large particles." Han et al. [39] established a numerical model of particle breakage by using the linear contact model and simulated the plane strain test. It was found that the particle breakage of rock fill firstly occurs in the particle with large size or contact force. Zhou et al. [40] studied the evolution process of particle breakage in the shearing process of sandy soil based on the discrete elements model. It was considered that the larger particles were preferentially broken and then became smaller particles. Hu et al. [41] performed triaxial shear tests on calcareous sand in Nansha Islands. It was found that the degree of particle breakage increases with the increase in the particle size; that is, large particle is crushed preferentially. As also stated by McDowell and Bolton [42], the anticrushing ability of particles is related to the particle size. Specifically, the larger the particle size is, the smaller the ability of anticrushing is; this conclusion might be one of the reasons for the "preferentially crushed of large particles." According to the distribution of microscopic stress of "preferential compression of large pores" explained previously, it was found that the "preferential crush of large particles" also related to the distribution of microscopic stress combined with the similar analytical method.

As shown in Figure 16, particles are taken as objects of observation. Firstly, the maximum particle size is taken as the observation scale, and only the largest particle can be observed in black, as shown in Figure 16(a). And the rest was the coexistence unit of particles and pores, expressed in light gray. The part of two sides of the unit (i.e., part B) was determined as relative flexible region with light gray, and the middle column contained the largest particle (i.e., part A) was defined as a relatively rigid region with dark gray, as shown in Figure 16(b).

According to the similar analysis presented previously, the stresses of the relative rigid and flexible region are consistent with the equations (2) and (3), respectively, where

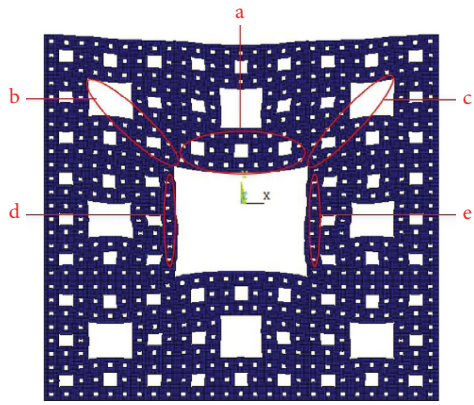

Figure 15: The deformation diagram of the large pore model under the maximum pressure.

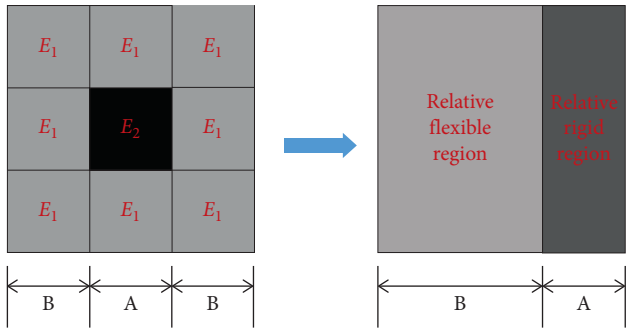

Figure 16: Particle elements.

A_r is the cross-sectional area of the relative rigid region and A_f is the cross-sectional area of the relative flexible region. Then, E_r and E_f can be expressed as

$$E_r = \frac{1}{((1/E_2)\Delta l + (2/E_1)\Delta l)/(3\Delta l)} = \frac{1}{(1/3E_2) + (2/3E_1)} = \frac{3E_1E_2}{E_1 + 2E_2} = \frac{3E_1}{(E_1/E_2) + 2}, \tag{8}$$

$$E_f = E_1. \tag{9}$$

Dividing equation (3) by equation (2) (that is, the ratio of stress of the relative rigid region to that of relative flexible region) gives

$$\frac{\sigma_r}{\sigma_f} = \frac{E_r}{E_f}. \tag{10}$$

As mentioned previously, $E_1 < E_2$, thus $E_1/E_2 < 1$. According to equations (8) and (9), it can be known that E_r is larger than E_f. Then combining with equation (10), it is easy to obtain that σ_r/σ_f is larger than 1, more precisely, σ_r is larger than σ_f.

It can be seen from above that the stress of the relative rigid region was larger than that of the relative flexible region; that is, the stresses of the large particles in the aggregate of soil were larger than those of the surrounding pores. As a consequence, the large particles were crushed firstly when it was subjected to external force.

By further analysis, it was found that if the total size of the unit in Figure 11 was maintained constant, the larger the particle size was, the larger the corresponding length Δl was, and the smaller the relative flexible region corresponding to length Δl was. According to equation (8), E_r increased with the increase of particle size. Combining with equation (10), the larger the maximum particle size was, the larger the ratio of σ_r to σ_f was, and the particle was easier to be crushed. On the contrary, if the relative compactness of the smaller particles on both sides of the maximum particle was lower, so the elastic modulus of the relative flexible region E_1 was smaller. According to equation (9), the smaller the E_f was, the greater the ratio of σ_r to σ_f was from equation (10). That is, the largest particles were easier to be crushed if the distribution of the smaller particles on both sides of the maximum particles were looser. As shown in Figure 17, the pebble iron wall of particles with different sizes is pushed by manpower. It is found that only smaller particles can be driven and the particles with the maximum particle size group are too firm to be moved. It is also stated that the stress of the maximum particle size group is larger and all of them are on the skeleton of particle size. Accordingly, the corresponding transfer path of main stress was drawn, as shown in Figure 18. Luo et al. [43] performed an one-dimensional consolidation test on sands. It was found that the structure of the large grain skeleton disappeared first after compression, and the fine particles were filled in the pores, which resulted in the deformation of sand. The conclusion in this paper was consistent with this discovery. These results preliminary explained that one of the main reasons for the "preferential crush of large particle" was that the large particle was subjected to higher stress.

4.4. Skeleton Stress across the Region of Larger Stiffness. As shown in Figures 12 and 17, it is found that the region with relatively larger stiffness undertakes the main skeleton stress of soil, which is consistent with the conclusion of equations (2)–(10). Consequently, skeleton stress generally avoids large pores (taking pores as the studied object) for clay soil; But for granular soil, skeleton stress will actively seek particles of the maximum particle size group (taking particles as the object of the study).

4.5. Self-Protection of Particles and Pores. The stress in the area of the broken large particles would be redistributed. Meanwhile the large particles would be deformed, which produced relative displacement with the surrounding particles. As a result, the stress of the large particles decreased relatively (that is, the stress of the surrounding particles increased accordingly), and thus the large particles were avoided further crushing. Some large particles were extremely "cunning"; only the surface was broken and a similar effect of stress reduction would be achieved, and thus wide areas of large particles were avoided to be damaged. In terms of clay, pores were taken as the studied object. After the large

Figure 17: Local photos of the pebble iron art fence.

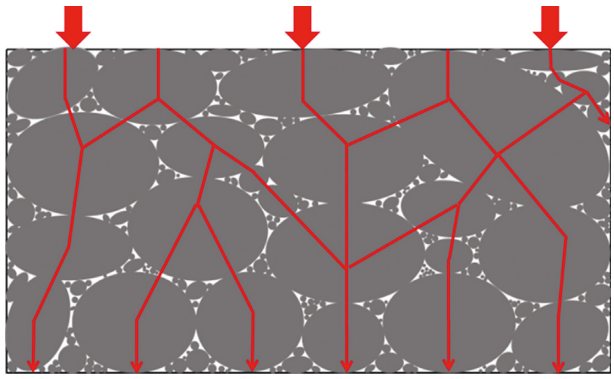

Figure 18: Schematic diagram of the main stress transmission way of the pebble iron art fence.

pores were deformed under pressure, the "arch stress distribution" would be produced in the upper part of the pore, as shown in part ② of Figure 12, where the stress of the upper part of the large pores was actually distributed to the two side edges. As a result, the "bending" of the upper part was reduced and the collapsing of large pores was avoided. Adjustment means of stress distribution were adopted to protect the large pore effectively.

5. Conclusion

The effect of consolidation pressure on microscopic pores of soil is convenient to be studied with physical tests, but the variation of area and shape of specific pores under different pressures is difficult to be tracked, and the internal mechanism of its variation law cannot be revealed. In this paper, the fractal structures of pore of clay soil were approximately simulated by the carpet model and its improved model, and the variation law of pore structure under different consolidation pressures was analyzed by using the ANSYS software. Combined with the graphic measurement function of IPP software, the concrete effect of consolidation pressure on pore structure was studied quantitatively. In addition, the phenomenon of "preferential compression of large pores" was verified, and its internal mechanism was explained by theoretical analysis combined with the results of numerical simulation on distribution of microscopic stress. Based on the results, many issues were discussed, such as the microscopic mechanism of the difference in horizontal and vertical permeability under compression deformation, the relationship between the changes of pore shape and microscopic stress, the preliminary principle of "preferential crush of large particles" for granular soil, skeleton stress across the region of larger stiffness, and the self-protection of particles and pores. The main conclusions are presented as follows:

(1) In the process of soil compression, the larger the stress was, the larger the compression was, and the pore area would be decreased, resulting in the ratio of particles increasing. Therefore, the fractal dimension would increase with the increase of stress. Furthermore, the fractal dimension has a linear relationship with the strain, which shows that fractal dimension can be the deformation parameter of soil during compression. The results of numerical simulation exhibit similar variation trends as the experimental data, which verified that the Sierpiński carpet model can approximately simulate the pore distribution of clay.

(2) Under the same pressure, the compression of large pore was much larger than that of small pores, and the phenomenon of "preferential compression of large pores" proposed in physical experiments was verified. The distribution of microscopic stress in soil was not uniform, and the larger the pore size was, the greater the compression stress on both sides and the bending in the upper part of the pore was, which was the internal reason of "preferential compression of large pores."

(3) The compression of pores with same size might be different under the same pressure when they were at different positions. In general, the compression in the upper part of the model was larger than that in the lower part, which explained why the permeability coefficient of horizontal soil was smaller than that of the vertical under compression deformation. The compression of the small pores on both sides and the oblique upper corner of large pores was larger than that of the pores with same size in the general position (especially near the large pores), which indicated that the deformation of the small pores was actually affected by the nearby large pores, which was related to the distribution of microscopic stress of soil.

(4) The variation laws of shape of pores with same size and different positions were different, which was greatly affected by the maximum pore size. Generally speaking, the pores near over large pores were produced distribution of arch stress resulting in less variation of pore shape, where the stress was smaller. Owing to the larger pressure, the pores on both sides of the large pores changed from the initial square to the approximate rectangle, while the shape of pores in the oblique upper corner of the

large pores generally changed from the initial square to parallelogram due to the large shear stress.

(5) According to the similarity analysis method of taking pores as the research object, it was found that the stress of the largest particle was greater than that of the smaller particle by taking particles as the research object, which was one of the internal reasons leading to the preferential crush of large particles.

(6) It was preliminary assumed that the region with large stiffness would be selected actively by the "skeleton stress" of clay and granular soil. In terms of clay, the "skeleton stress" would generally avoid large pores, but the large particles of granular soil would be chosen by "skeleton stress" actively.

(7) Large particles and pores have self-protective mechanisms. The distribution of "arch stress" was formed over the large pores to reduce the bending of the soil and prevent the upper soil from collapsing. The surface of the particles was broken, which resulted in the redistribution and reduction of stress, whereas further crushing of particles were avoid.

Data Availability

The data used to support the findings of this study are available from the corresponding author upon request.

Conflicts of Interest

The authors declare that there are no conflicts of interest regarding the publication of this paper.

Acknowledgments

The research was funded by the National Key R&D Program of China (no. 2016YFC0502208), National Natural Science Foundation of China (no. 51608182), and Research Project of Hubei Provincial Education Department (no. D20161405) which are gratefully acknowledged.

Supplementary Materials

S1 table is corresponding to Figure 5. S2 table is corresponding to Figure 6. S3 table is corresponding to Figure 8. S4 table is corresponding to Figure 9. S5 table is corresponding to Figure 10. S6 table is corresponding to Figure 11. (*Supplementary Materials*)

References

[1] A. S. Gylland, H. Rueslåtten, H. P. Jostad, and S. Nordal, "Microstructural observations of shear zones in sensitive clay," *Engineering Geology*, vol. 163, pp. 75–88, 2013.

[2] J. Zhang, J. Zhu, L. Huang, and Y. Xia, "Evolution of micro pore structure of soft clay and its fractal features under consolidation," *Journal of Hydraulic Engineering*, vol. 39, no. 4, pp. 394–400, 2008.

[3] L. Zhang, W. Ma, and C. Yang, "Investigation on the effects of freeze-thaw action on the pore water pressure variation of soils," *Journal of Offshore Mechanics and Arctic Engineering*, vol. 140, no. 6, article 062001, 2018.

[4] X. Tan, J. Liu, L. Zhang, and J. Cai, "Fractal analysis of stress sensitivity of permeability in porous media," *Fractals*, vol. 23, no. 2, article 1550001, 2015.

[5] R. Liu, B. Li, Y. Jiang, H. Jing, and L. Yu, "On the relationship between equivalent permeability and fractal dimension of dual-porosity media subjected to fluid-rock reaction under triaxial stresses," *Fractals*, vol. 26, no. 5, article 1850072, 2018.

[6] G. Lei, S. Mo, Z. Dong, C. Wang, and W. Li, "Theoretical and experimental study on stress-dependency," *Fractals*, vol. 26, no. 2, article 1840010, 2018.

[7] K. Terzighi, *Theoretical Soil Mechanics*, Geological Publishing House, Beijing, China, 1960.

[8] Y. Wu, "Quantitative approach on micro-structure of engineering clay," *Bulletin of the Chinese Academy of Geological Science*, vol. 23, no. 2, pp. 143–151, 1991.

[9] M. R. Cox and M. Budhu, "A practical approach to grain shape quantification," *Engineering Geology*, vol. 96, no. 1-2, pp. 1–16, 2008.

[10] A. Tarantino and E. De Col, "Compaction behaviour of clay," *Géotechnique*, vol. 58, no. 3, pp. 199–213, 2008.

[11] D. N. Arnepalli, S. Shanthakumar, B. Hanumantha Rao, and D. N. Singh, "Comparison of methods for determining specific-surface area of fine-grained soils," *Geotechnical and Geological Engineering*, vol. 26, no. 2, pp. 121–132, 2007.

[12] M. Oualmakran, B. C. N. Mercatoris, and B. François, "Pore-size distribution of a compacted silty soil after compaction, saturation, and loading," *Canadian Geotechnical Journal*, vol. 53, no. 12, pp. 1902–1909, 2015.

[13] Y. Gao, D. Sun, and A. Zhou, "Hydromechanical behaviour of unsaturated soil with different specimen preparations," *Canadian Geotechnical Journal*, vol. 53, no. 6, pp. 909–917, 2016.

[14] E. Romero and P. H. Simms, "Microstructure investigation in unsaturated soils: a review with special attention to contribution of mercury intrusion porosimetry and environmental scanning electron microscopy," *Geotechnical and Geological Engineering*, vol. 26, no. 6, pp. 705–727, 2008.

[15] M. Hattab, T. Hammad, J.-M. Fleureau, and P.-Y. Hicher, "Behaviour of a sensitive marine sediment: microstructural investigation," *Géotechnique*, vol. 63, no. 1, pp. 71–84, 2013.

[16] X. Zhang and L. Kong, "Study of pore characteristics of offshore clay by SEM and MIP and NA methods," *Rock and Soil Mechanics*, vol. 34, no. S2, pp. 134–142, 2013.

[17] U. Khalid, C. C. Liao, G.-L. Ye, and S. K. Yadav, "Sustainable improvement of soft marine clay using low cement content: a multi-scale experimental investigation," *Construction and Building Materials*, vol. 191, pp. 469–480, 2018.

[18] L. R. Stingaciu, L. Weihermueller, S. Haberpohlmeier, S. Stapf, H. Vereecken, and A. Pohlmeier, "Determination of pore size distribution and hydraulic properties using nuclear magnetic resonance relaxometry: a comparative study of laboratory methods," *Water Resources Research*, vol. 46, no. 11, pp. 2387–2392, 2010.

[19] S. Tomioka, T. Kozaki, H. Takamatsu et al., "Analysis of microstructural images of dry and water-saturated compacted bentonite samples observed with X-ray micro CT," *Applied Clay Science*, vol. 47, no. 1-2, pp. 65–71, 2010.

[20] Z. H. Nie, K. Li, and J. Xia, "Research on coarse-grained soil collapsibility in Gobi region," *Advanced Materials Research*, vol. 446-449, no. 4, pp. 1450–1453, 2012.

[21] J. Wang, P. Li, Q. Gu, Y. Xu, and T. Gu, "Changes in tensile strength and microstructure of loess due to vibration," *Journal of Asian Earth Sciences*, vol. 169, pp. 298–307, 2019.
[22] R. K. Matthew, E. R. Hannah, D. M. Austin, and L. K. Steven, "Investigation of cyclic liquefaction with discrete element simulations," *Journal of Geotechnical and Geoenvironmental Engineering*, vol. 140, no. 12, pp. 1–13, 2014.
[23] S. Zhao, T. M. Evans, and X. Zhou, "Effects of curvature-related DEM contact model on the macro- and micro-mechanical behaviours of granular soils," *Géotechnique*, vol. 68, no. 12, pp. 1085–1098, 2018.
[24] A. Sufian, A. R. Russell, and A. J. Whittle, "Evolving pore orientation, shape and size in sheared granular assemblies," *Granular Matter*, vol. 21, no. 4, pp. 1–13, 2019.
[25] H. Farroukh, T. Mnif, F. Kamoun, L. Kamoun, and F. Bennour, "Stabilization of clayey soils with Tunisian phosphogypsum: effect on geotechnical properties," *Arabian Journal of Geosciences*, vol. 11, no. 23, pp. 1–11, 2018.
[26] N. Zainuddin, N. Z. Mohd Yunus, M. A. M. Al-Bared, A. Marto, I. S. H. Harahap, and A. S. A. Rashid, "Measuring the engineering properties of marine clay treated with disposed granite waste," *Measurement*, vol. 131, pp. 50–60, 2019.
[27] P. Li, W. Xie, R. Y. S. Pak, and S. K. Vanapalli, "Micro-structural evolution of loess soils from the Loess Plateau of China," *Catena*, vol. 173, pp. 276–288, 2019.
[28] O. Cuisinier and L. Laloui, "Fabric evolution during hydro-mechanical loading of a compacted silt," *International Journal for Numerical and Analytical Methods in Geomechanics*, vol. 28, no. 6, pp. 483–499, 2004.
[29] C. Zhou and C. Mu, "Relationship between micro-structural characters of fracture surface and strength of soft clay," *Chinese Journal of Geotechnical Engineering*, vol. 27, no. 10, pp. 1136–1141, 2005.
[30] X. Zhang and C. Wang, "Microstructural change of soft clay before and after one-dimensional compression creep," *Chinese Journal of Geotechnical Engineering*, vol. 32, no. 11, pp. 1688–1694, 2010.
[31] G. Tao, J. Zhang, and X. Zhuang, "Influence of compression deformation on the soil-water characteristic curve and its simplified representation method," *Journal of Hydraulic Engineering*, vol. 45, no. 10, pp. 1239–1246, 2014.
[32] Y. Tan, L. Kong, and A. Guo, "Research on effect of compaction on pore size distribution of laterite soil," *Rock and Soil Mechanics*, vol. 31, no. 5, pp. 1427–1430, 2010.
[33] H. Qian, J. Wang, and Y. Luo, *Collapsible Loess Foundation*, Building Industry Press, Beijing, China, 1985.
[34] H. Xie, "Fractal pores and fractal particles of rock and soil materials," *Advances in Mechanics*, vol. 23, no. 2, pp. 145–164, 1993.
[35] B. Yu and J. Li, "Some fractal characters of porous media," *Fractals*, vol. 9, no. 3, pp. 365–372, 2001.
[36] G. Tao and J. Zhang, "Two categories of fractal models of rock and soil expressing volume and size-distribution of pores and grains," *Chinese Science Bulletin*, vol. 54, no. 23, pp. 4458–4467, 2009.
[37] M. Wu, J. Liu, X. Lv, D. Shi, and Z. Zhu, "A study on homogenization equations of fractal porous media," *Journal of Geophysics and Engineering*, vol. 15, no. 6, pp. 2388–2398, 2018.
[38] T. Wang, T. Yang, and J. Lu, "Influence of dry density and freezing-thawing cycles on anisotropic permeability of loess," *Rock and Soil Mechanics*, vol. 37, no. S1, pp. 72–78, 2016.
[39] H. Han, W. Chen, and Z. Qiu, "Numerical simulation of two-dimensional particle flow in broken rockfill materials," *Chinese Journal of Geotechnical Engineering*, vol. 38, no. S2, pp. 234–239, 2016.
[40] B. Zhou, Y. Huang, and H. Wang, "Study of evolution of sand crushability based on discrete elements method," *Rock and Soil Mechanics*, vol. 35, no. 9, pp. 2709–2716, 2014.
[41] B. Hu, R. Wang, and Q. Meng, "The experimental investigations of the crush of calcareous sand particles under the condition of triaxial," *China Marine Society*, vol. 3, pp. 367–369, 2009.
[42] G. R. McDowell and M. D. Bolton, "On the micromechanics of crushable aggregates," *Géotechnique*, vol. 48, no. 5, pp. 667–679, 1998.
[43] T. Luo, L. Liu, and Y. Yao, "Description of critical state for sands considering particle crushing," *Chinese Journal of Geotechnical Engineering*, vol. 39, no. 4, pp. 592–600, 2017.